1
Thermally Sensitive Microgels: From Basic Science to Applications

He Cheng and Guangzhao Zhang

1.1
Introduction

A thermally sensitive microgel is a microscopic three-dimensional gel network (10^2 nm) consisting of crosslinked macromolecular chains that can undergo volume "phase" transitions in response to temperature. Since the first thermally sensitive microgel – poly(*N*-isopropylacrylamide) (PNIPAM) microgel – was synthesized in 1986 via precipitation polymerization [1], microgels have received increasing interest because of their applications in hollow thermosensitive capsules, heat storage, thermoregulated textiles [2], *in vivo* diagnostics [3], and gene or drug delivery [4]. Moreover, since a microgel can vary in size from tens of nanometers to several micrometers, it exhibits unique physical properties between those of a polymer coil and a macroscopic gel [5]. In fact, because the swelling or shrinking of a microgel is caused by conformational changes of the subchains between two neighboring crosslinking points inside the gel network, the coil-to-globule transition of individual linear polymer chains can help us to understand the swelling/shrinking of a thermally sensitive microgel.

In terms of the mean field theory of Flory [6], the coil-to-globule region in the phase diagram is sandwiched between the θ-region and the phase boundary [7]. Stockmayer predicted that a flexible linear homopolymer chain can switch its conformation from an expanded coil to a collapsed globule if the solvent quality gradually changes from good to poor but will still remain in the one-phase region [8]. However, the coil-to-globule transition of single chain is difficult to observe experimentally because of the very narrow temperature window resolved [9–18]. Grosberg and Kuznetsov [19] predicted a two-stage kinetic for the collapse of a single chain, namely, a fast crumpling of the unknotted chain followed by a slow knotting of the collapsed polymer chain. The two-stage kinetic was experimentally observed by Chu and coworkers [20, 21] in the study of the collapse of single polystyrene chain. In 1996, Wu *et al.* [22, 23] successfully observed the coil-to-globule transition of thermally sensitive PNIPAM homopolymer chains in water, which has a lower critical solution temperature (LCST) at ∼32 °C. The study provides fundamentals for studying PNIPAM microgels.

Hydrogel Micro and Nanoparticles, First Edition. Edited by L. Andrew Lyon and Michael Joseph Serpe.

The mechanisms for volume phase transition, internal motion, aggregation, and non-ergodic phenomena are fundamental problems in gel systems. We will introduce the developments in the fields by using microgel as a model system. Section 1.2 is about the theoretical background. Section 1.3 deals with the basic physics of microgels. The applications of microgels are presented in Section 1.4.

1.2 Theoretical Background

1.2.1 Thermodynamics of Volume Phase Transition

The swelling or shrinking of polymer gels is a fundamental and classic problem in polymer physics. Dusek and coworkers [24, 25] showed that certain polymer gels can undergo a discontinuous volume change or the so-called volume phase transition with temperature. Supposing the chemical potential of the solvent is in equilibrium with that of the swollen gel,

$$\frac{\Delta\mu_1}{RT} = \ln a_1 = \ln(1-\varphi_2) + \varphi_2 + \chi_T\varphi_2^2 + \zeta(\varphi_2^{1/3} < \alpha^2>_0 - \kappa\varphi_2) \tag{1.1}$$

the chemical potential per equivalent segment ($\Delta\mu_2/n$) of the network polymer is,

$$\frac{\Delta\mu_2}{nRT} = -\varphi_1 + \chi_T\varphi_1^2 + \zeta\left[< \alpha^2>_0 \left(\frac{\varphi_2^{-2/3}}{2} + \varphi_2^{-1/3} - \frac{3}{2}\right) - \kappa(\ln\varphi_2 + \varphi_1)\right] \tag{1.2}$$

where the subscripts 1 and 2 denote the solvent and the polymer, respectively, $n = V_2/V_1$ with V being the partial molar volume, φ is the volume fraction, χ_T is the Flory–Huggins polymer–solvent interaction parameter depending on the temperature T, $\zeta = \varrho V_1/M_c$, where ϱ and M_c are respectively the density of the dry gel and the average molar mass of the subchain between two neighbor crosslinking points. The isotropic deformation factor of the gel network $<\alpha^2>_0$ is defined as the ratio of the mean square end-to-end distance of the chains in a dry network to that of unperturbed free chains. $0 < \kappa < 1$, depending on the models [26–28].

When two phases with different concentrations coexist, the equations $\mu_1 = \mu'_1$ and $\mu_2 = \mu'_2$ have a solution outside the unstable region wherein $\partial\Delta\mu_2/\partial\varphi_2 > \partial\Delta\mu_1/\partial\varphi_2$. Inserting Equations 1.1 and 1.2 into $\mu_1 = \mu'_1$ and $\mu_2 = \mu'_2$, one can calculate the curves describing the composition of the gel, namely χ_T versus φ_2. The coexistence of the swollen and the collapsed phases requires that χ_T is sufficiently high but $<\alpha^2>_0$ and M_c are sufficiently low. However, a low M_c means a high crosslinking density or a high $<\alpha^2>_0$. Therefore, it is practical to choose a gel system with a strong interaction between the polymer network and solvent (i.e., a higher χ_T) to study the volume phase transition.

Hydrogels are often used to test the theoretical prediction in experiments because of their higher χ_T values. Lightly crosslinked PNIPAM gels show a sharp volume

change at ~33 °C, which was taken as the discontinuous volume phase transition [29–34]. However, a continuous volume change was also observed for PNIPAM and other hydrogels [35–38]. Clearly, on the basis of Equations 1.1 and 1.2, a discontinuous volume phase transition is expected as long as the equations $\mu_1 = \mu'_1$ and $\mu_2 = \mu'_2$ have a solution outside the unstable region. It should be noted that Li and Tanaka [35] showed that as the crosslinking density of a bulk PNIPAM gel decreases, a continuous volume change transits into a discontinuous one.

1.2.2 Internal Motion

Pecora showed that when an infinitely dilute polymer solution is illuminated by a coherent and monochromatic laser light beam, the spectral distribution of the light scattered from a flexible polymer chain can be written as [39]

$$S(q,\varpi) = (1/2\pi)\int \mathrm{e}^{-i\varpi t}\mathrm{e}^{-q^2 D|t|}S(q,t)\mathrm{d}t \tag{1.3}$$

where ω is the angular frequency difference between the scattered and the incident light, D is the translational diffusion coefficient of individual chains, and $S(q,t)$ is generally expressed as

$$S(q,t) = < (1/N^2)\sum_{i=0}^{N}\sum_{j=0}^{N}\mathrm{e}^{-iq\cdot[r_i(0)-r_j(t)]} > \tag{1.4}$$

which is due to the interference of the scattered light from different segments within a long polymer chain made of N such segments, where $\boldsymbol{r}_i(0)$ is the position of the ith segments at time 0 and $\boldsymbol{r}_j(t)$ is the position of the jth segment at time t, both referred to the center of mass of the polymer.

To perform the ensemble average in $S(q,t)$, a model for the internal motion of a chain is needed. By incorporating the Oseen–Kirkwood–Riseman hydrodynamic interaction into the bead-and-spring model, Perico, Piaggio, and Cuniberti have shown [40, 41]

$$\begin{aligned} S(q,\varpi) = {} & P_0(x)L(\varpi, q^2 D) + \sum_{\alpha=1}^{N} P_1(x,\alpha)L(\varpi, q^2 D + \Gamma_\alpha) \\ & + \sum_{\alpha=1}^{N}\sum_{\beta=1}^{N} P_2(x,\alpha,\beta)L(\varpi, q^2 D + \Gamma_\alpha + \Gamma_\beta) \\ & + \sum_{\alpha=1}^{N}\sum_{\beta=1}^{N}\sum_{\gamma=1}^{N} P_3(x,\alpha,\beta,\gamma)L(\varpi, q^2 D + \Gamma_\alpha + \Gamma_\beta + \Gamma_\gamma) + \cdots \end{aligned} \tag{1.5}$$

where $x = (qR_g)^2$, and the function

$$L(\varpi,\Gamma) = \frac{2\Gamma}{2\pi(\varpi^2 + \Gamma^2)} \tag{1.6}$$

This represents the ω-normalized Lorentzian distribution with Γ being the half-width at half-height, that is, the line width, and P_n ($n = 0,1,\ldots$) determines the contribution of each Lorentzian to the line width distribution $G(\Gamma)$ of the scattered light. The zeroth-order of $P_0(x)$ represents the contribution from the translational diffusion, $P_1(x,\alpha)$ is the first-order contribution of the αth internal mode, $P_2(x,\alpha,\beta)$ is the second-order contribution of the αth and βth internal modes, and so on. When $x < 1$, the spectral distribution is measured in the long-wavelength regime and the polymer chain is viewed as a point. Accordingly, $P_0(x)$ is dominant in $S(q,\omega)$. As x increases, the light probes a portion of the chains and the contributions from $P_1(x,\alpha)$, $P_2(x,\alpha,\beta)$, and other higher order terms become more important. Perico and coworkers have numerically shown that $P_2(x,1,1)$ is the largest contribution to $S(q,\omega)$ among all Lorentzian terms associated with the internal modes [40, 41].

According to the theories for a flexible polymer coil in the free-draining [42] and nondraining limits [40, 41], When $x > 1$, $S(q,t)$ mainly depends on the first five relaxation processes, namely, a pure translational term plus four principal internal motions. In decreasing order of the contributions to the spectrum, Equation 1.5 in the time domain at $x > 1$ can be written as

$$S(q,t) = \sum_{n=0}^{\infty} P_n \mathrm{e}^{-\Gamma_n t} \tag{1.7}$$

where P_n (the numeric values) in the range of $1 \leq x \leq 10$ have been calculated by Perico and coworkers [40, 41]. On the basis of the Zimm model [43],

$$\Gamma_n/(Dq^2) = \frac{0.293RT\lambda_n' R_g^2}{xD\eta_0 M[\eta]}. \tag{1.8}$$

where $RT/(D\eta_0) = 6\pi R_h N_A$ (the Stokes–Einstein equation) so that

$$\Gamma_n/(Dq^2) = \frac{5.52\lambda_n' R_g^2 R_h}{xM[\eta]} = \frac{5.52\lambda_n'(R_g/R_h)^2}{x}\frac{R_h^3}{M[\eta]} \tag{1.9}$$

where $[\eta]$ is the intrinsic viscosity, λ'_n are the eigenvalues in the Zimm model [44], $M[\eta]$ is a measure of hydrodynamic volume, $M[\eta]/R_h{}^3 = \Phi$ (the Flory constant), which is widely used as the universal calibration in gel permeation chromatography (GPC), and R_g/R_h depends weakly on the nature of polymer and solvent for flexible linear polymer chains in a good solvent.

In a modern dynamic laser light scattering (DLS) experiment, the intensity–intensity time correlation function of the scattered light can be measured from which $S(q,t)$, and the Fourier transform of $S(q,\omega)$ is determined.

1.2.3 Dynamics of Microgel

In static laser light scattering (SLS), the angular dependence (15–150°) of the excess absolute time-averaged scattered intensity, that is, the Rayleigh ratio $R_{vv}(q)$, which leads to the weight-averaged molar mass M_w and the z-averaged root mean square

radius of gyration $<R_g{}^2>_z{}^{1/2}$ (or written as $<R_g>$) of scattering objects and the scattering vector q as [45],

$$\frac{Kc}{R_{vv}(q)} = \frac{1}{M_w}\left(1 + \frac{1}{3} < R_g^2 > q^2 - \cdots\right) + 2A_2c - \cdots \tag{1.10}$$

In DLS, the intensity–intensity time correlation function $g^{(2)}(t,q)$ in the self-beating mode was measured, where t is the decay time. The $g^{(2)}(t,q)$ function can be related to the normalized first-order electric field time correlation function $|g^{(1)}(t,q)|$ via the Siegert relation as $g^{(2)}(t,q) = B[1 + \beta|\, g^{(1)}(t,q)|^2]$ where B ($\equiv <I(0)>^2$) is the measured baseline. For the broadly distributed relaxation spectrum, $|g^{(1)}(t,q)|$ is related to a characteristic relaxation time distribution $G(\tau)$, that is, $|g^{(1)}(t,q)| \equiv <E(0,q)E^*(t,q)>/<E(0,q)E^*(0,q)> = \int G(\tau)e^{-t/\tau}d\tau$, where $G(\tau)$ can be calculated from the Laplace inversion of the measured $g^{(2)}(t,q)$ [51]. For a pure diffusive relaxation, the characteristic decay time, $\Gamma = 1/\tau$, can be related to the translational diffusion coefficient D by $(\Gamma/q^2)_{C\to 0, q\to 0} = D$ or a hydrodynamic radius $R_h = k_BT/6\pi D\eta$ with k_B, T, and η being the Boltzmann constant, the absolute temperature and the solvent viscosity, respectively [46, 47].

In a semi-dilute solution or a solution undergoing the crosslinking reaction, $|g^{(1)}(t,q)|$ can also be analyzed by a single-exponential function combined with a stretched exponential function to take care of the additional slow relaxation as follows [48–51],

$$\left|g^{(1)}(t,q)\right| = A_f \exp\left(-\frac{\tau}{<\tau_c>_f}\right) + A_s \exp\left(-\frac{\tau}{<\tau_c>_s}\right)^b \tag{1.11}$$

where A and $<\tau_c>$ are the intensity weighting and the average characteristic decay time, respectively; subscripts "s" and "f" denote the fast and slow modes, respectively; and $0 < b < 1$, a constant related to the distribution width of the characteristic decay time. Note that $A_f + A_s = 1$. Strictly speaking, when using Equation 1.11, we have assumed that the two relaxation modes are "monodisperse," which is not true in reality [52].

For a non-ergodic system, the time-averaged scattered light intensity, $<I>_T$, is different from the position-averaged ones, and it contains both static and dynamic contributions, $<I>_s$ and $<I>_d$, namely [53],

$$<I>_T = <I>_s + <I>_d \tag{1.12}$$

where $<I>_d$ is independent of the sample position but $<I>_s$ not. Therefore, at a given q, for each chosen sample position, we can measure one $<I>_T$ and one normalized intensity–intensity time correlation function $g^{(2)}(t,q)$. $g^{(2)}(t,q)$ can be written as [53–56],

$$\begin{aligned}\left|g^{(2)}(t,q)\right| = &\left(\frac{<I>_d}{<I>_T}\right)^2 \exp\left(-2Dq^2t\right) \\ &+ 2\left(\frac{<I>_d}{<I>_T}\right)\left[1 - \left(\frac{<I>_d}{<I>_T}\right)\right]\exp\left(-Dq^2t\right)\end{aligned} \tag{1.13}$$

For a non-ergodic system at a given q, one can measure the time-averaged scattered intensity from different sample positions to obtain an ensemble-averaged scattered intensity, $<I>_E$. Note that for a given q, $<I>_T$ depends on the sample position, but not $<I>_E$ by its definition: $<I>_E = \Sigma <I>_{T,i}/N$, where I=1,2,. . .,N, and N is the number of the positions measured. Only in an ergodic system, $<I>_E$=$<I>_T$. In the dynamic measurement, the initial slope of each $\ln g^{(2)}(t,q)$ vs. t leads to an apparent diffusion coefficient D_A in the range of $D/2 < D_A < D$. It is known that D and $<I>_d$ are related to D_A and $<I>_T$ as [53, 54]

$$\frac{<I>_T}{D_A} = \frac{2<I>_T}{D} - \frac{<I>_d}{D} \tag{1.14}$$

Experimentally, for each chosen sample position at a given q, one can measure one $<I>_T$ from SLS and calculated one D_A from $g^{(2)}(t,q)$ measured in DLS. Therefore, on the basis of Equation 1.13, D and $<I>_d$ can be respectively obtained from the slope and the intercept of the plot of $<I>_T/D_A$ vs. $<I>_T$ by measuring at a number of sample positions.

1.2.4
Kinetics Calculation of Reversible Aggregation

Diffusion-limited cluster–cluster aggregation (DLCA) follows a second-order growth kinetics, and the coagulation kernel is independent of the size of resultant aggregates [57–59]. On the other hand, the fragmentation follows first-order kinetics, and its rate is also independent of the size of the aggregates [57]. Assuming that at any given time t, $N(t)$ is the total number of the microgel clusters, including individual microgels in which the aggregation number is only one, we can write the changing rate of $N(t)$ as [60]

$$\frac{dN(t)}{dt} = -k_a[N(t)]^2 + k_f\left[N_{microgel} - N(t)\right] \tag{1.15}$$

where $N_{microgel}$ is the total molar number of initial microgels in the dispersion, a constant for a given microgel concentration, and k_a and k_f are the rate constants of aggregation and fragmentation, respectively. As $t \to \infty$, $dN(t)/dt \to 0$ for a system at a dynamic equilibrium. In this way, the ratio k_a/k_f can be solved in terms of $N(\infty)$ and $N_{microgel}$, that is, $k_a/k_f = [N_{microgel} - N(\infty)]/N^2(\infty)$. Using the two boundary conditions, $N(0)$ and $N(\infty)$, we can analytically solve Equation 1.15 as

$$\ln\frac{[N(t)-N(\infty)][N_{microgel}N(0)-N(0)N(\infty)+N_{microgel}N(\infty)]}{[N(0)-N(\infty)][N_{microgel}N(t)-N(t)N(\infty)+N_{microgel}N(\infty)]} = -st \tag{1.16}$$

where $s = k_f[(2N_{microgel} - N(\infty))/N(\infty)]$. Experimentally, $N(0)$ and $N(\infty)$ can be determined from the weight-averaged molar masses of the microgel clusters ($M_{w,c}(0)$ and $M_{w,c}(\infty)$) at $t \to 0$ and $t \to \infty$, respectively. This is because the total microgel mass

(M_{total}) for a given dispersion is a constant, namely, $M_{total}=M_{w,m}N_{microgel}=M_{w,c}(t)\ N(t)$. Since $N(t)$ is proportional to the reciprocal of $M_{w,c}(t)$, Equation 1.16 can be rewritten as

$$\frac{[M_{w,c}(t)-M_{w,c}(\infty)][M_{w,c}(\infty)+M_{w,c}(0)-M_{w,m}]}{[M_{w,c}(0)-M_{w,c}(\infty)][M_{w,c}(\infty)+M_{w,c}(t)-M_{w,m}]}=\exp(-st) \tag{1.17}$$

The left side of Equation 1.17 can be measured experimentally.

1.3
Basic Physics of Microgels

A thermally sensitive microgel provides a model system in polymer physics. On one hand, its three-dimensional crosslinked polymer network shows typical viscoelastic property. On the other hand, a microgel with a dimension between polymer coil and gel shows a combination of their physical properties.

1.3.1
Volume Phase Transition

The volume phase transition theory states that the phase transition temperature depends on the length of the subchain between two neighboring crosslinking points inside the gel, so it is helpful to compare the results for linear chains and spherical microgels [61–64].

Figure 1.1 shows the temperature dependence of the expansion factor α_h [$\equiv<R_h>/<R_h>_\Theta$], where $<R_h>_\Theta$ is the hydrodynamic radius at $T=\Theta$. The volume change associated with the temperature dependence of the hydrodynamic

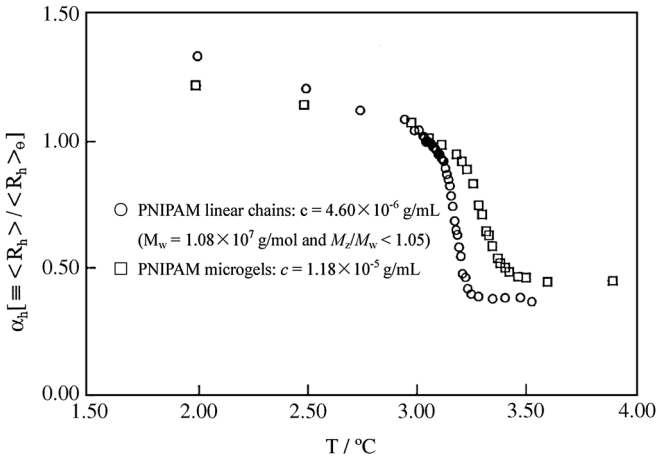

Figure 1.1 Expansion factor α_h [$\equiv<R_h>/<R_h>_\Theta$] as a function of temperature for the PNIPAM microgels and individual chains, where $<R_h>_\Theta$ is the hydrodynamic radius at $T=\Theta$. Reprinted with permission from [64], Wu, C. *Polymer* 39, 4609, 1998. © 1998 Elsevier Science.

radii of both the linear chains and the spherical microgels is continuous. It is well known that for a linear polymer chain in solution its phase transition temperature has molecular weight dependence [6]. For a given polymer solution with a LCST, the higher the molecular weight, the lower the phase transition temperature. For a polydisperse sample, polymer chains with different lengths undergo phase transition at different temperatures, leading to a continuous transition. Figure 1.1 shows that the microgels swell less than the linear chains in the good solvent region. The phase transition temperature of the microgel is ~1.5 °C higher than that of the PNIPAM linear chains. At a low temperature, either the microgels or the linear chains are swollen. As temperature increases, the segment–segment interaction becomes strong, and they start to collapse. However, the detailed mechanism is different. When a gel is swollen, the elasticity would retard the chain expansion in good solvent. In a poor solvent, the elasticity prevents its collapse. Therefore, a linear chain collapses easier than a gel.

Figure 1.1 also indicates that linear chains have a sharper volume change than microgels. Tanaka *et al.* [29] attributed this to the polydispersity of microgels. However, according to Equations 1.1 and 1.2, the phase transition temperature or χ_T is not related to the gel dimension but the subchain length or M_c because the temperature is a thermodynamic intensive property.

Figure 1.2 shows a simulation of χ_T vs. φ based on Equations 1.1 and 1.2, where χ_T decreases as ζ decreases, that is, as M_c decreases. Therefore, the transition temperature decreases as M_c increases. Clearly, the linear chains have a lower transition temperature because of their much higher average molecular weight ($M_w = 1.08 \times 10^7\,g\,mol^{-1}$) compared to the subchains ($M_c \sim 10^4\,g\,mol^{-1}$) inside the microgels.

Normally, the subchains inside a polymer gel have a broad molecular weight (length) distribution and a gel network can be visualized as a set of subnetworks with different M_c. As temperature varies, the subnetwork with a longer subchain undergoes phase transition before that with a shorter subchain. Thus, different parts of the

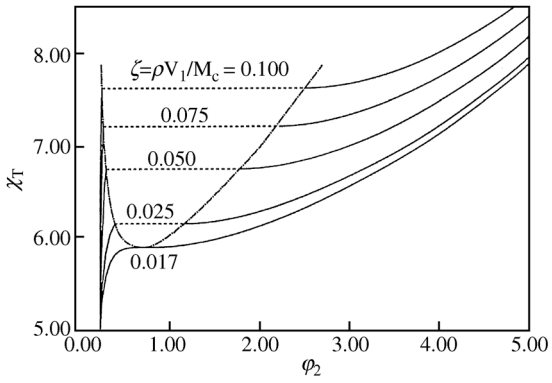

Figure 1.2 Plot of χ_T versus φ_2 for a polymer gel based on Equations 1.1 and 1.2, where we have chosen $\kappa = 0.5$, $<\alpha^2>_0 = 0.04$, and $\zeta = \varrho V_1/M_c$. Reprinted with permission from [65], Wu, C. and Zhou, S.Q. *Macromolecules* 30, 574, 1997. © 1997 American Chemical Society.

gel network experience phase transition at different temperatures. The fact that a transparent PNIPAM gel changes into a milky gel in phase transition indicates the microscopic inhomogeneity. Therefore, the volume phase transition of a polymer gel should be practically continuous because the subchains normally have a broad chain length distribution. With the subchain inhomogeneity concept, it is also possible to explain that higher homogeneity gels with a lower crosslinking density display a discontinuous volume phase transition.

In principle, the discontinuous volume phase transition predicted on the basis of Equations 1.1 and 1.2 is correct if M_c is a constant or the subchains have a uniform chain length. However, it will be extremely difficult to prepare such a gel, if not impossible. Note that the use of one average M_c in Equations 1.1 and 1.2 is very successful in many other predictions; for example, the relation between a shear modulus G and M_c, that is, $G = RT\varrho\Phi/M_c$, where Φ is the volume ratio of the dry and swollen gels.

The discontinuous volume phase transition of bulk PNIPAM gel can be explained as follows. As discussed above, longer subchains inside the gel undergo phase transition before shorter subchains. Then, the shrinking of a small amount of longer subchains initially cannot alter the overall dimensions of a bulk gel because of its shear modulus, but can build up stress inside the gel. The stress will gradually increase until the shear modulus cannot maintain the macroscopic shape of the gel, and the overall dimension of the gel will change abruptly, leading to a discontinuous macroscopic volume change with temperature. As for the microgels with an average radius of $\sim$0.1–0.2 μm, the shear modulus plays a minor role so that its dimension changes continuously when the stress increases. Generally, it takes several days for a bulk gel to attain the swelling or shrinking equilibrium [66]. In the process, unless the temperature is kept to be a constant with a fluctuation less than $\pm$0.01 °C and the incremental temperature is less than 0.1 °C, a continuous volume phase change can be taken to be a discontinuous one. In contrast, it takes less than one second for microgels to reach equilibrium, so the study of microgels is more straightforward.

1.3.2 Internal Motion

Dynamics of linear flexible chains such as polystyrene (PS), polyisoprene (PIP), and PNIPAM in solution have been examined. Here, we focus on the internal motion in PNIPAM linear chains and microgels in good and Θ solvents [67].

1.3.2.1 Internal Motions in Good Solvent

Figure 1.3 shows typical plots of $G(\Gamma/q^2)$ vs. Γ/q^2 for individual PNIPAM linear chains at 15 °C and different x. $G(\Gamma/q^2)$ changes with x: at $x < 1$, there exists only a single narrow peak which corresponds to the Brownian motion of PNIPAM linear chains in solution. When $x \sim 1$, a second peak appears at larger Γ/q^2, while the first peak basically retains its position. This second small peak is related to the internal motions of PNIPAM chains. The first peak becomes broader and shifts to larger Γ/q^2

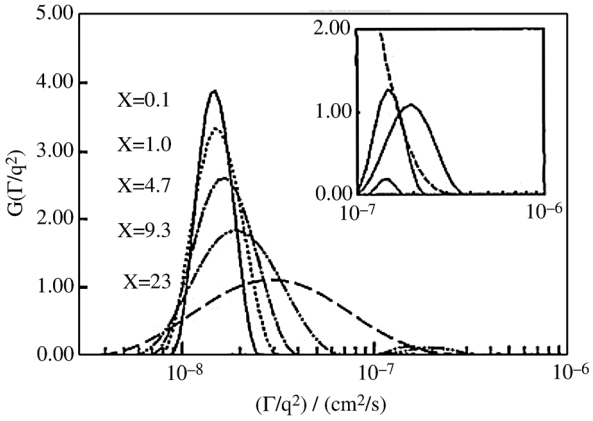

Figure 1.3 Typical line width distributions $G(\Gamma/q^2)$ of the PNIPAM linear chains at 15 °C. The insert shows a 10-fold enlargement of the second peak in the range of $10^{-7} < \Gamma/q^2 < 10^{-6}\,\mathrm{cm^2\,s^{-1}}$. Reprinted with permission from [68], Wu, C. and Zhou, S.Q. *Macromolecules* 29, 1574, 1996. © 1996 American Chemical Society.

with x. This is understandable because the observation length scale ($1/q$) is much shorter than R_g at larger x and the observation is well inside the microgel particle. More internal motions with larger Γ contribute to the relaxation and mix with the translational diffusion in the measured spectrum. Finally, two peaks merge into one broader peak because the line width associated with D increases with q, while the line widths related to the internal motions are independent of q.

Figure 1.4 shows a plot of $<\Gamma>_{peak2}/(Dq^2)$ vs. x, where $<\Gamma>_{peak2}$ is the average line width of the second peak in Figure 1.3. For comparison, previous experimental data

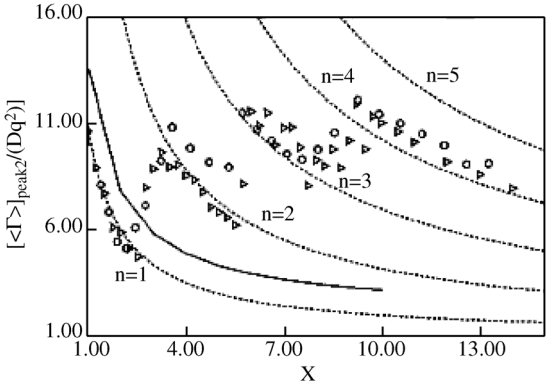

Figure 1.4 Plots of the reduced average line width $<\Gamma>_{peak2}/(Dq^2)$ vs. x. Open circles: PNIPAM linear chains in water at $T=15$ °C; triangles: polystyrene in toluene at $T=20$ °C [108]. The dashed lines are predicted in [108], and the full lines are calculated from Equations 1.7 and 1.8. Reprinted with permission from [68], Wu, C. and Zhou, S.Q. *Macromolecules* 29, 1574, 1996. © 1996 American Chemical Society.

about polystyrene are also plotted here [69]. Clearly, the two plots follow a similar pattern. The dotted lines in Figure 1.4 show the predicted $[1 + 2\Gamma_n/(Dq^2)]$ dependence on x for polystyrene in toluene [69]. As discussed in Section 1.2, Equation 1.9 predicts that Γ_n is independent of polymer and solvent for polymers in good solvents. Equation 1.9 also reveals that $\Gamma_n/(Dq^2)$ decreases as x increases for a given temperature, which explains the shift of the average position of the second peaks. Figure 1.4 shows that the two sets of results from completely different polymer/solvent systems follow a very similar pattern, which indicates that the prediction of Equation 1.9 is essentially correct.

The average line width $<\Gamma>_{int}$ associated with the internal motions can be calculated by using the numeric values of P_n in Refs [40, 41] and the values of Γ_n calculated from Equation 1.8 for polystyrene in toluene at 20 °C [69]. The plot of $<\Gamma>_{int}/(Dq^2)$ vs. x (the solid line) is illustrated in Figure 1.4. If Equation 1.7 was right, $<\Gamma>_{int}/(Dq^2)$ would follow the solid line. But Figure 1.4 shows a clear deviation between the data and the solid line. On the other hand, Figure 1.4 shows that the experimental data have a tendency to respectively follow the dotted lines of $n = 1$ in $1 < x < 3$; $n = 2$ in $3 < x < 6$; $n = 3$ in $6 < x < 10$; $n = 4$ in $10 < x < 15$. Thus, Γ_1, Γ_2, Γ_3, and Γ_4 in different ranges of x can be estimated by analyzing $<\Gamma>_{int}/(Dq^2)$ in Figure 1.4 with an assumption of $<\Gamma>_{int}/(Dq^2) = 1 + 2<\Gamma>_n/(Dq^2)$. For $x > 15$, two peaks in Figure 1.3 merge into a broader peak, which makes it difficult to get a precise $<\Gamma>_{peak2}$ value from the spectral distribution $G(\Gamma)$. So we stopped the second peak analysis at $x > 15$ to avoid any ambiguity. It shows the internal motion in either polystyrene or PNIPAM is related to $2\Gamma_n$ or $\Gamma_n + \Gamma_n$ dominates the relation measured in DLS in different range of x. $\Gamma_n + \Gamma_n$ relaxation implies a self-coupling of nth order internal motion based on Equations 1.5 and 1.7. So far, the nature of the internal motion remains unclear. Energetically, it is easier to excite the internal motions associated with Γ_1 and $4\Gamma_1$ than those with $2\Gamma_2$, $2\Gamma_3$, and $2\Gamma_4$. What is observed is $2\Gamma_2$ instead of Γ_1 and $4\Gamma_1$, indicating that DLS can only measure a certain kind of internal motion because of the observation length scale $1/q$. Therefore, not all internal motions can be observed by DLS in a certain range of x, although they do exist.

A similar phenomenon is also observed in PNIPAM microgels. Figure 1.5 shows $G(\Gamma/q^2)$ vs. Γ/q^2 plot for the spherical PNIPAM microgel particles as a function of x at 15 °C. $G(\Gamma/q^2)$ is independent of x at $x < 13$ and only a single, narrow peak is observed. When $x > 13$, a very small second peak associated with the internal motions of the microgel network appears. By comparison with Figure 1.3, we can see that the internal motions for the linear chains start to contribute to $G(\Gamma)$ when $1/q \sim R_g$, while the internal motions for the particles appear only when $1/q \sim R_g/(13)^{1/2} \sim R_g/3.6$. Thus the former involve the entire chain, while the latter are only related to a fraction of the microgel network.

1.3.2.2 Internal Motions in Θ and Poor Solvents

Figure 1.6 shows that the extrapolation of time-averaged scattered light intensity at different temperatures to zero angle leads to an identical value, indicating no change in the weight-averaged molar mass, or collapse of individual linear PNIPAM chains

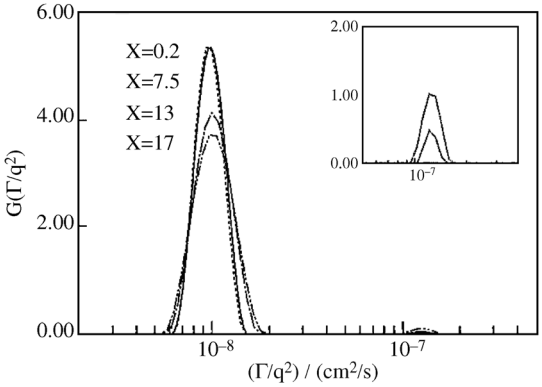

Figure 1.5 Typical plots of $G(\Gamma/q^2)$ vs. Γ/q^2 for the microgel particles at 15 °C. The insert shows a 10-fold enlargement of the second peak at $\Gamma/q^2 \sim 10^{-7}\,\mathrm{cm^2\,s^{-1}}$. Reprinted with permission from [68], Wu, C. and Zhou, S.Q. *Macromolecules* 29, 1574, 1996. © 1996 American Chemical Society.

without interchain association. Thus, the internal motions of individual chains at different temperatures can be studied, especially under the Θ temperature and in poor solvent conditions.

Figure 1.7 shows how the internal motions vary with the relative observation length scale (x) at 31.0 °C (Θ temperature) where the chains are not fully collapsed yet, and the line width (Γ) is scaled with translational diffusion coefficient (D) and scattering vector (q). It is worth noting that here $1/q$ is compared with R_g. For $x < 1$, that is, $1/q > R_g$, each chain behaves just like a structureless point so that we only see its Brownian motion. When $x \geq 1$, a second peak related to the internal motions appears in the measured line width distribution, which relaxes 10–20 times faster than the translational diffusion.

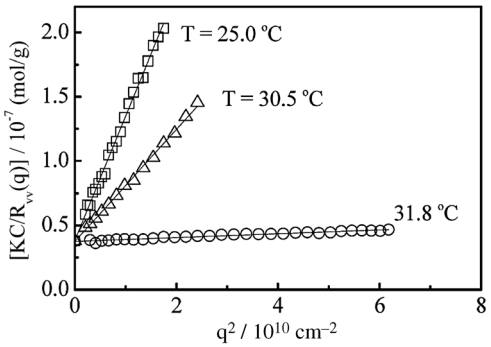

Figure 1.6 Scattering vector (angular)-dependent time-averaged scattered light intensity (Rayleigh ratio) of PNIPAM linear chains in water at three different temperatures. Reprinted with permission from [70], Dai, Z.J. and Wu, C. *Macromolecules* 43, 10064, 2010. © 2010 American Chemical Society.

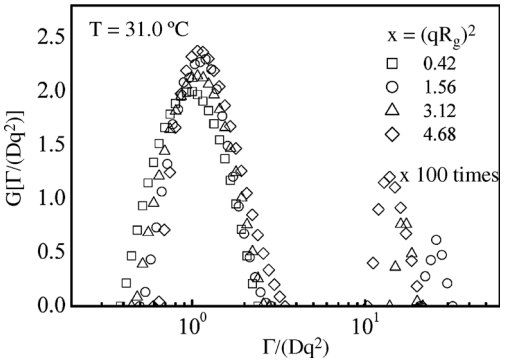

Figure 1.7 *x*-dependent Dq^2-scaled line width distributions $G(\Gamma/Dq^2)$ of PNIPAM linear chains in water, where the peak related to internal motions is enlarged by a factor of 100 times for a better view. Reprinted with permission from [70], Dai, Z.J. and Wu, C. *Macromolecules* 43, 10064, 2010. © 2010 American Chemical Society.

A parallel study of PNIPAM spherical microgels has also been conducted. The microgel collapses much less than the linear chains, presumably due to the crosslinking. In contrast to linear chains where internal motion is observed at $x \sim 1$, the second peak related to the internal motion of the microgels is much weaker and appears only when $x \geq 8$ at 25.0 °C; thus we can only observe their internal motions when $1/q \sim 50\,\text{nm} \leq \langle R_g \rangle/3$, instead of at $1/q \sim \langle R_g \rangle$, implying that the thermal energy can excite the entire linear chain with its longest normal mode, but only a small portion of a gel network with a dimension of ~50 nm.

Figure 1.8 shows that the internal motion at a smaller x (~5–6) can be observed at 31.5 °C, implying that the thermal energy excites a large portion of the gel

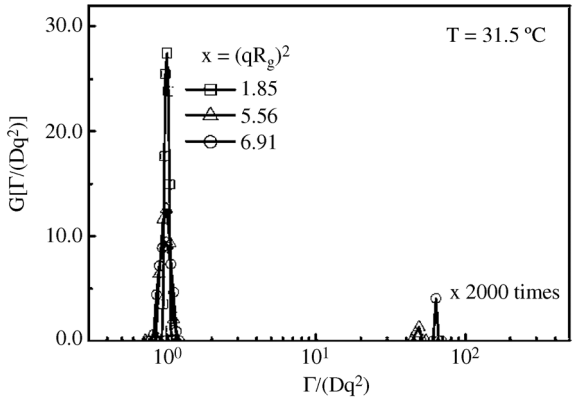

Figure 1.8 *x*-dependent q^2-scaled line width distributions $G(\Gamma/Dq^2)$ of PNIPAM microgels in water, where the peak related to internal motions is enlarged by a factor of 2000 for a better view. Reprinted with permission from [70], Dai, Z.J. and Wu, C. *Macromolecules* 43, 10064, 2010. © 2010 American Chemical Society.

network to undergo the internal motion and the microgel becomes softer. If we imagine that the gel network is made of small uniform meshes with a dimension of ~10 nm on the basis of the crosslinking density, we can estimate that the internal motions only involve about $\sim 10^2$ of such meshes from the minimum $1/q$. Note that such measured internal motions are slower than the relaxation of the subchains ("blobs") of a macroscopic gel network with a similar crosslinking density but faster than the translational diffusion of individual microgels in the dispersion.

1.3.3
Dynamics of Cation-Induced Aggregation of Thermally Sensitive Microgels

Despite a great deal of effort, the kinetics and dynamics of complex formation among polyelectrolytes and cations or protein are still poorly understood due to the complexity of the systems. These complex systems exhibit quite different responses to various experimental conditions. Here, we present the kinetics and dynamics of cation-induced aggregation of microgels in dilute solution, and the complexation between microgels and protein. The effects of temperature, pH, and ionic strength have been examined [71, 72].

1.3.3.1 Salt-Induced Complexation

Microgels made of poly(*N*-vinylcaprolactam) (PVCL) and a few per cent of sodium acrylate (SA) were used as a model system to study the cation-induced reversible and controllable aggregation of colloid particles because PVCL exhibits continuous shrinking in the range of 25–40 °C. The presence of SA can increase the extent of its swelling and shifts the temperature at which it shrinks to a higher level [73, 74]. It is known that certain alkaline earth ions and heavy metal ions can specifically interact with carboxylic groups [75, 76], which can lead to cation–polyanion complexation, even at a very low cation concentration [77]. This is probably because the addition of metal ions to an aqueous solution of polyanions alters the hydration or disrupts oriented water molecules near the chain [78–80].

Figure 1.9 shows the temperature dependence of the average hydrodynamic radius $\langle R_h \rangle$ and apparent weight-averaged molar mass ($M_{w,app}$) of linear P(VCL-*co*-SA) chains and microgels in 0.03 M $CaCl_2$ aqueous solution. In the range 25–31.8 °C, the microgels shrink with temperature but $M_{w,app}$ stays constant, indicating no inter-microgel aggregation. At ~32 °C, $\langle R_h \rangle$ and $M_{w,app}$ increase sharply, revealing a clear inter-microgel aggregation. Linear chains can entangle and complex with each other via the interaction between Ca^{2+} and COO^- to form a hyperbranched structure. For the microgels, when the transition temperature is reached, PVCL becomes hydrophobic and the microgel starts to collapse but the hydrophilic COO^- groups tend to stay on the periphery of the microgel. The complexation between Ca^{2+} and COO^- sticks the microgels together.

Figure 1.10 shows the effects of different cations on the P(VCL-*co*-SA) microgels as a function of temperature [81, 82]. Clearly, Na^+ has the weakest effect on microgels, while Hg^{2+} leads to profound shrinking. This is understandable because the

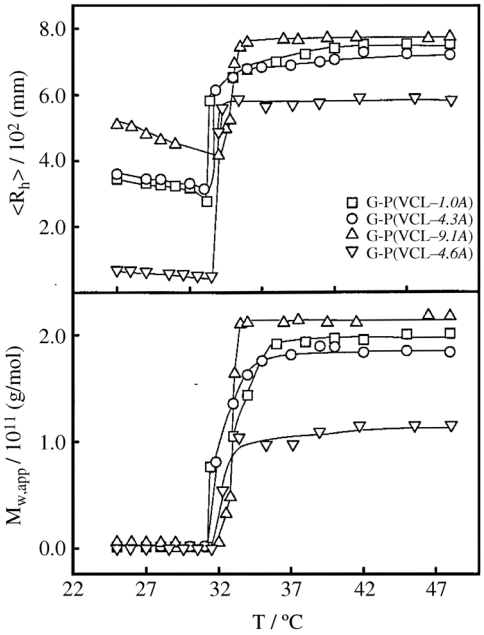

Figure 1.9 Temperature dependence of the average hydrodynamic radius $\langle R_h \rangle$ and apparent weight-averaged molar mass ($M_{w,app}$) of linear P (VCL-*co*-SA) chains and spherical microgels with the presence of Ca^{2+}, where $[Ca^{2+}] = 0.03$ M. Reprinted with permission from [71], Peng, S.F. and Wu, C.J. *Phys. Chem. B* 105, 2331, 2001. © 2001 American Chemical Society.

presence of monovalent Na^+ can only increase the ionic strength and reduce electrostatic repulsion between carboxylic groups. However, divalent cations can also pull two carboxylic groups together so that they can induce greater shrinking of the microgels. The fact that the molar mass of the microgels ($M_{w,\,microgel}$) remains a constant indicates that there is no interparticle complexation. In other words, the interaction between cations and microgels at 25 °C is intra-microgel. Figure 1.10 shows that in terms of the effect of different cations on the shrinking of the microgel, $Hg^{2+} > Cu^{2+} > Ca^{2+}$. This is related to the ion-specificity.

We have also studied the sorting of oppositely charged microgels, P(NIPAM-*co*-SA) and poly(*N*-isopropylacrylamide-*co*-vinylbenzyl trimethylammonium chloride) (P(NIPAM-*co*-VT)). In the absence of salt, P(NIPAM-*co*-SA) and P(NIPAM-*co*-VT) microgels in the mixture do not aggregate but shrink upon heating. The addition of monovalent cations does not affect the aggregation. In the presence of divalent metal ions, the heating leads to the association of P(NIPAM-*co*-SA) microgels via the complexation of metal ions and carboxyl groups on the microgel surface when the temperature approaches the LCST. Further increasing the temperature over the LCST results in the adsorption of P(NIPAM-*co*-VT) microgels on the P(NIPAM-*co*-SA) aggregate via the electrostatic attraction so that a core–shell structure, with a

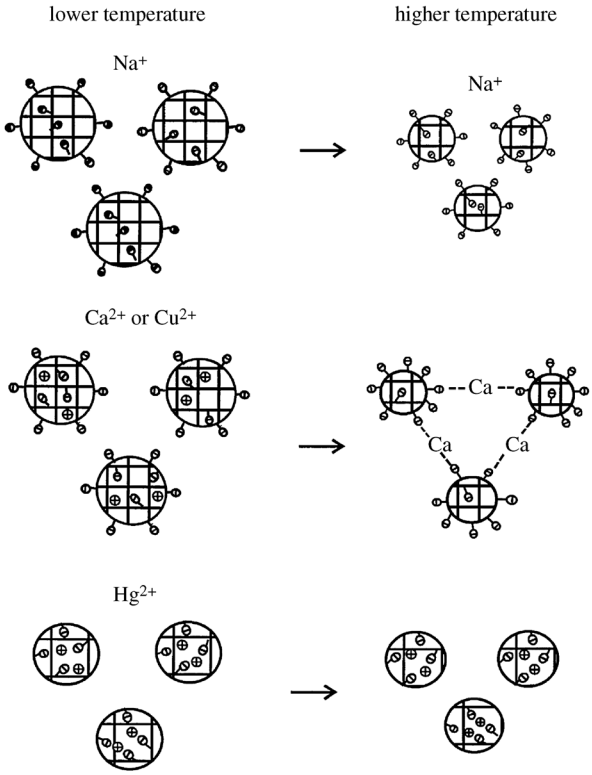

Figure 1.10 Schematic of effects of different cations and temperature on P(VCL-*co*-SA) microgels. Reprinted with permission from [82], Peng, S.F. and Wu, C. *Polymer* 42, 6871, 2001. © 2001 Elsevier Science.

P(NIPAM-*co*-SA) core and a P(NIPAM-*co*-VT) shell forms, resembling the biological cell-sorting.

Figure 1.11 shows the hydrodynamic radius distributions $f(R_h)$ of P(NIPAM-*co*-SA) and P(NIPAM-*co*-VT) microgels and their mixture in the presence of $CaCl_2$ at 51 °C, $\langle R_h \rangle$ values are ~40, 120, and 420 nm, respectively. The larger size of the mixture clearly indicates that the oppositely charged microgels form mixed aggregates with a narrow size distribution.

The structure of the microgel aggregates has been directly observed by high-resolution transmission electron microscopy (TEM) (Figure 1.12). Since metal ions can enhance the electron density contrast, the Ca^{2+} complexed with carboxyls makes a contrast between P(NIPAM-*co*-SA) and P(NIPAM-*co*-VT) domains. Clearly, the aggregates have a core–shell structure. The inset shows the image of the aggregates stained by iodine vapor. A boundary can be clearly observed. It is formed by P(NIPAM-*co*-VT) microgels because iodine can bind with $[N(CH_3)_3]^+$ but cannot with Ca^{2+}. Thus, P(NIPAM-*co*-SA) and P(NIPAM-*co*-VT) microgels form the core and shell of an aggregate, respectively. The core–shell structure indicates that the

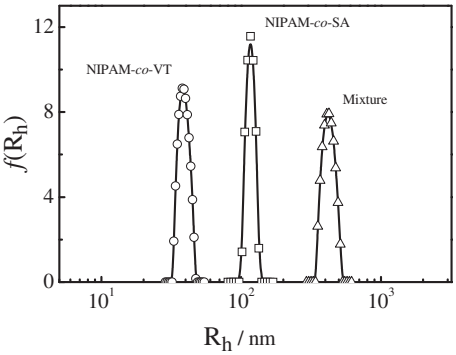

Figure 1.11 Hydrodynamic radius distributions $f(R_h)$ of P(NIPAM-*co*-SA) and P (NIPAM-*co*-VT) microgels and their mixture (1/1, w/w) in the presence of Ca^{2+} at 51 °C, where the concentrations of microgels and Ca^{2+} are 5.0×10^{-5} g mL^{-1} and 0.03 M, respectively. Reprinted with permission from [83], Hou, Y., Ye, J., Wei, X.L., and Zhang, G.Z. *J. Phys. Chem. B* 113, 7457, 2009. © 2009 American Chemical Society.

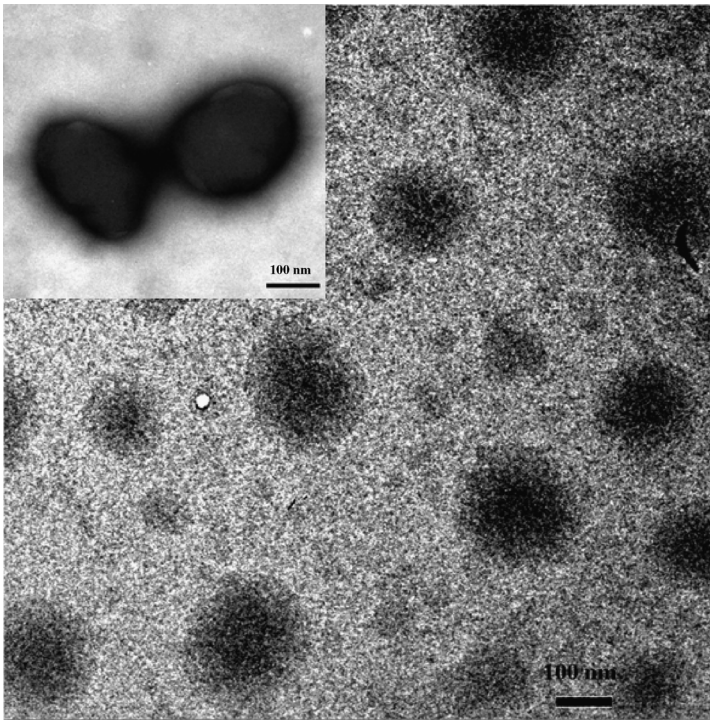

Figure 1.12 TEM image of P(NIPAM-*co*-SA) and P(NIPAM-*co*-VT) microgel aggregates at 51 °C. The inset shows the image of the aggregates stained by I_2 vapor. Reprinted with permission from [83], Hou, Y., Ye, J., Wei, X.L., and Zhang, G.Z. *J. Phys. Chem. B* 113, 7457, 2009. © 2009 American Chemical Society.

oppositely charged microgels exhibit sorting behavior during the aggregation, which is determined by the difference in Ca^{2+} adhesion between the unlike microgels.

1.3.3.2 Complexation Between Microgels and Protein

Complexation of a polyelectrolyte and a protein can provide an insight into its physicochemical properties, such as biocompatibility for other applications [84, 85]. In biopolymers, the complexation can modify their biological activities such as blood clotting and muscular contraction [86, 87]. In spite of a great deal of effort, the details of the complexation and stabilization are still missing because of its complex nature.

Figure 1.13 shows that when the gelatin/microgel molar ratio [G]/[M] is less than $\sim 3.4 \times 10^4$ and in the absence of Ca^{2+}, both $\langle R_h \rangle$ and $M_{w,app}$ of the microgel/gelatin complexes only slightly increase at about 32 °C, revealing that each complex contains at most two microgels on average. Further increasing temperature leads to a gradual decrease of $\langle R_h \rangle$, but $M_{w,app}$ is nearly independent of temperature in the same range, indicating the shrinking of the microgels without inter-microgel association. For mixtures with a higher molar ratio, $\langle R_h \rangle$ decreases monotonously with temperature in the whole temperature range studied. The increase in the average chain density ($\langle \varrho \rangle$) of the microgel/gelatin complexes with temperature in the range ~32–45 °C reflects the shrinking of the microgels inside the complex. Note that at high temperatures, $\langle \varrho \rangle$ increases as the [G]/[M] ratio decreases, further indicating that more microgels inside each complex can provide a stronger shrinking force and lead to a more compact structure at high temperatures.

Figure 1.14 shows that the complexation is more profound in the presence of Ca^{2+} compared with that shown in Figure 1.13. Both $\langle R_h \rangle$ and $M_{w,app}$ increase as the [G]/[M] ratio decreases, indicating that gelatin chains act as a stabilizer, presumably because of the absorption of gelatin chains on the microgel surface. Note that the complexation occurs at a similar temperature regardless of the gelatin concentration. This clearly shows that when the microgel is in its shrunk state (hydrophobic), most of the carboxylic groups are forced to locate on the microgel surface so that Ca^{2+} can bind the microgels and gelatin chains through the carboxylic groups. On average, each complex contains 20–70 microgels and the average density of the complexes is in the range 0.13–0.22 g cm^{-3} at temperatures higher than ~32 °C. The deceases in N_{agg} [$\equiv M_{w,aggregate}/M_{w,microgel}$] and $\langle \varrho \rangle$ with [G]/[M] further indicate that the adsorption of gelatin chains on the microgel surface reduces the compexation of the microgels.

1.3.3.3 Aggregation of Spherical Microgels

Aggregation of colloidal particles in dispersion has been extensively studied because it is important in both theory and practice; for example, in the production of chemical toners and the treatment of wastewater [89–96]. Two limiting regimes have been identified: the diffusion-limited cluster–cluster aggregation (DLCA) and the reaction-limited cluster–cluster aggregation (RLCA) [97, 98]. One of the features distinguishing between them is the different fractal dimensions (ν) of the resultant aggregates, that is, different scaling between the mass (M) and size (R) of the aggregates, $M \sim R^{\nu}$. The regime is essentially governed by the sticking efficiency between two collided

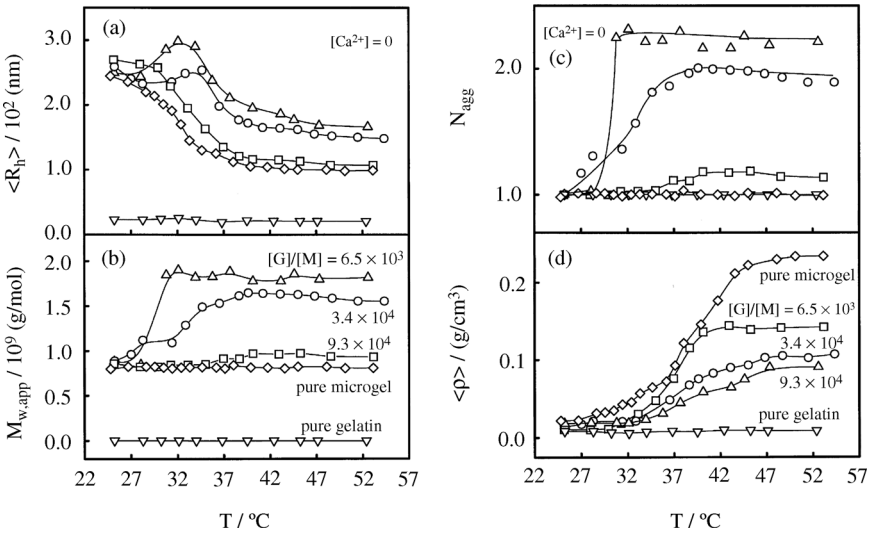

Figure 1.13 Temperature dependence of (a) average hydrodynamic radius $\langle R_h \rangle$; (b) apparent weight-averaged molar mass ($M_{w,app}$); (c) average aggregation number (N_{agg}); and (d) average chain density $\langle \varrho \rangle$ of the microgel/gelatin complexes, where [G]/[M] is the initial gelatin/microgel molar ratio and $\langle \varrho \rangle$ is defined as $M_{w,app}/[(4/3)\pi\langle R_h \rangle^3]$. Reprinted with permission from [88], Peng, S.F. and Wu, C. *Polymer* 42, 7343, 2001. © 2001 Elsevier Science.

particles. Experimentally, a combination of different scattering techniques allows us to study the formation and structures of colloidal aggregates over a wide size range [99–101].

The Ca^{2+}/COO^- complexation can induce a fractal aggregate at 32.5 °C. As expected, the extent of the aggregation for a given Ca^{2+} concentration increases with the ionic content because each COO^- group acts as a "sticker" in the interparticle or interchain aggregation via the $Ca^{2+}(COO^-)_2$ complexation. Figure 1.15 shows that the scattering intensity $I(q)$ of the resultant aggregates is dependent on the scattering vector q as $I(q) \sim q\alpha$ with α=1.7–1.9 for spherical microgels and α=2.4–2.5 for linear chains, indicating that the aggregation of spherical microgels follows the DLCA process, but the aggregation of linear chains might be described by the RLCA mechanism. For spherical microgels, the slight decrease of α with the COO^- groups indicates that the structure of the aggregates made of microgels with fewer COO^- groups is relatively more open and less uniform.

Note that the reversible processes of aggregation or fragmentation happen simultaneously. Therefore, a kinetic model should be established. As we know, Ca^+-induced spherical P(VCL-*co*-SA) microgel aggregation is a DLCA process, and it follows a second-order growth kinetics, whose coagulation kernel is independent of the size of the resultant aggregates. On the other hand, fragmentation is a first-order kinetics whose rate is also independent of the size of the aggregates. Therefore, Equation 1.17 can be used to fit both the heating and cooling data.

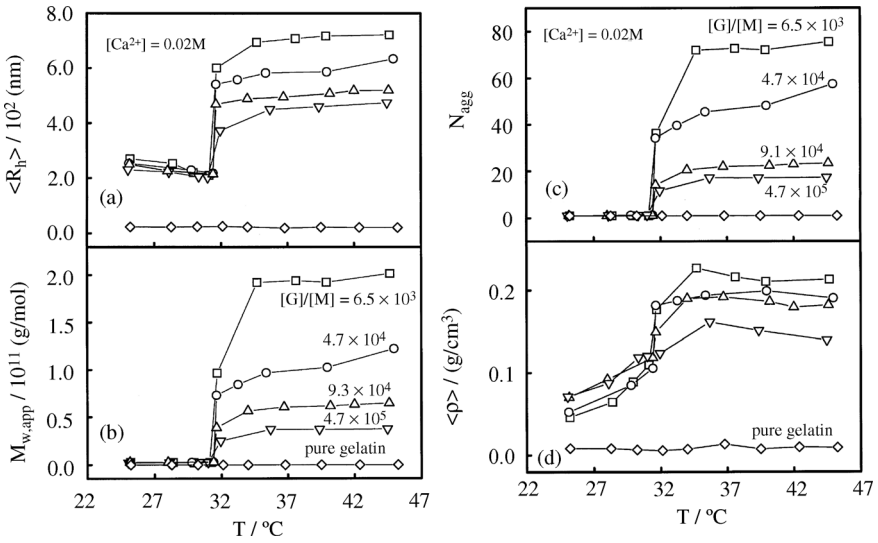

Figure 1.14 Temperature dependence of (a) average hydrodynamic radius $\langle R_h \rangle$; (b) apparent weight-averaged molar mass ($M_{w,app}$); (c) average aggregation number (N_{agg}); and (d) average chain density $\langle \varrho \rangle$ of the microgel/gelatin complexes. Reprinted with permission from [88], Peng, S.F. and Wu, C. *Polymer* 42, 7343, 2001. © 2001 Elsevier Science.

Figure 1.16 shows that aggregation dominates the initial process at higher temperatures but the fragmentation rate gradually increases with time. Note that each cluster contains ~230 microgels on average when $t \rightarrow \infty$. Such an aggregation process is reversible if the temperature decreases to ~35 °C. At lower temperatures each cluster contains only about two and about four microgels on average,

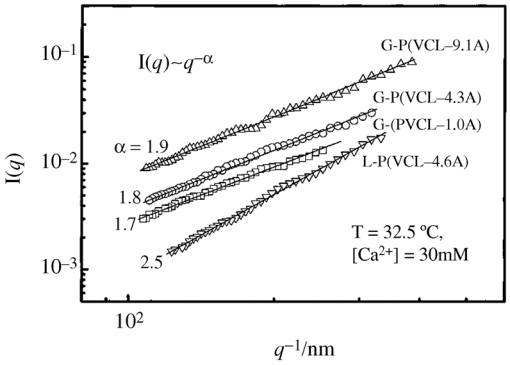

Figure 1.15 Double-logarithmic plots of scattering intensity I(q) vs. scattering vector q for resultant aggregates made of different spherical microgels and linear chains, where $[Ca^{2+}]$=30 mM and T=32.5 °C. Reprinted with permission from [81], Peng, S.F. and Wu, C. *Macromolecules* 34, 6795, 2001. © 2001 American Chemical Society.

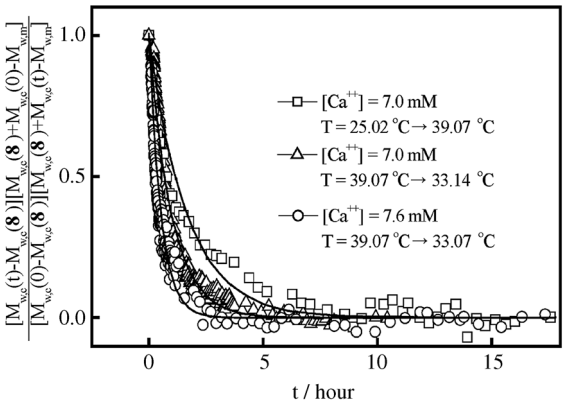

Figure 1.16 Time dependence of function $\{[M_{w,c}(t)-M_{w,c}(\infty)][M_{w,c}(\infty)+M_{w,c}(0)-M_{w,m}]\}/\{[M_{w,c}(0)-M_{w,c}(\infty)][M_{w,c}(\infty)+M_{w,c}(t)-M_{w,m}]\}$ after a microgel dispersion ($c=2.6\times10^{-6}\,g\,mL^{-1}$) was heated or cooled to different temperatures. The solid lines represent the best fitting on the basis of Equation 1.17. Reprinted with permission from [60], Cheng, H., Wu, C., and Winnik, M.A. *Macromolecules* 37, 5127, 2004. © 2004 American Chemical Society.

respectively, indicating that the microgel clusters formed at higher temperature are essentially redissolved.

1.3.4
Non-Ergodic and Ergodic Phenomena of Physical Crosslinked Gel

The network structure of a gel can be formed by either a chemical or a physical gelation process. In a chemical process, linear chains gradually turn into branched clusters, and then clusters are interconnected by covalent bonds to form a network structure. In a physical process, various forces such as van der Waals forces, electrostatic attraction, and hydrogen bonding can be employed to bind polymer chains to form a network. Therefore, the sol–gel transition in physical gels is often reversible [102–105].

It is well known that in the formation of normal chemical gels short linear chains are first formed, then large branched clusters, and finally a network, where the clusters ("islands") are interconnected to form a "continent," while the solvent "sea" is changed into "lakes" [106–109]. In principle, such an inhomogeneous clustering structure could be avoided if long polymer chains uniformly distributed in a solution are randomly associated to form a physical gel. Recently, DLS has been used to study a non-ergodic solid-like medium such as polymer gels or colloidal glasses [110], wherein the Brownian motions of scattering elements are limited around fixed average positions. One obvious characteristic of the non-ergodicity is the appearance of speckles; thus, the scattered intensity depends on the sample position. It is now generally known that the concentration fluctuation inside a gel comprises both static and dynamic parts. The inhomogeneous static part represents a frozen structure,

while the dynamic fluctuation presumably reflects diffusive relaxation [111–119]. The concept of non-ergodicity has led to the development of several relevant methods for the analysis of the dynamic properties of gels [54, 120, 121].

A novel hydrogel, in which billions of small spherical swollen PNIPAM microgels (~100 nm) in a concentrated dispersion are close-packed into a macroscopic three-dimensional gel network, has been developed. Inside each microgel, the polymer chains were chemically crosslinked, but the microgels were close-packed by physical interaction. This is why we named it a "hybrid" gel. It resembles a glass in which atoms or small molecules are replaced by "large" spherical microgels. There are several advantages of using this hybrid gel as a model system to study the volume–concentration-induced sol–gel transition and structures of physical gels. For example, the structural inhomogeneity resulting in the microgel preparation is limited in volume ($\sim 100 \times 100 \times 100\ nm^3$), and it is so small in comparison with the wavelength of light that it does not show up in laser light scattering. Also, as building blocks, these microgels are narrowly distributed and well characterized. Moreover, such a gelation is completely thermally reversible without any hysteresis. Using a combination of SLS and DLS, we studied a series of such hybrid gels formed at different gelling rates and temperatures. The main finding is that the observed static non-ergodicity is not intrinsic but strongly depends on how the microgels (clusters) are packed. Therefore, it can be completely suppressed if there are no large voids among the microgels. On the other hand, the dynamic fluctuation is almost not influenced by the static non-ergodicity.

Figure 1.17 shows that in the gel state, the time-averaged scattered intensity $\langle I \rangle_T$ randomly varies with sample position [122]. In contrast, the scattering speckle pattern disappears at 30 °C because the bulk hybrid gel melts into microgel dispersion (i.e.,

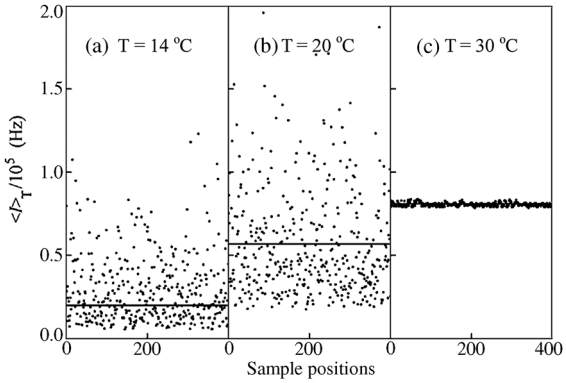

Figure 1.17 Sample position dependence of time-averaged scattered light intensity $\langle I \rangle_T$ of hybrid PNIPAM gel after the microgel dispersion was quickly cooled from 40 °C to different gelling temperatures, where the scattering angle (θ) is 90°, and each solid line represents an ensemble-averaged scattered light intensity $\langle I \rangle_E$ defined as $\sum \langle I \rangle_{T,i}/N$ with N being the total number of randomly chosen sample positions. Reprinted with permission from [122], Zhao, Y., Zhang, G.Z., and Wu, C. *Macromolecules* 34, 7804, 2001. © 2001 American Chemical Society.

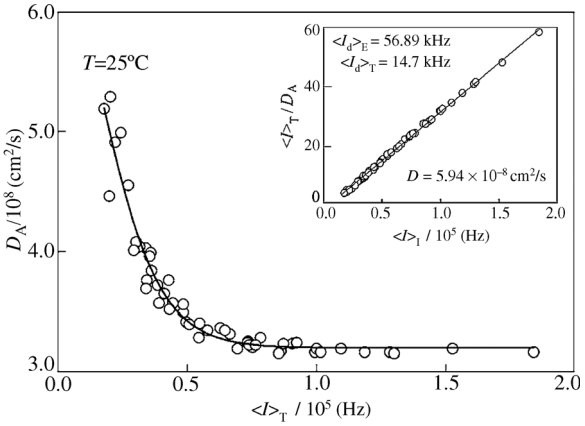

Figure 1.18 Time-averaged scattered light intensity $\langle I \rangle_T$ dependence of apparent diffusion coefficient D_A of the hybrid gel formed at 20 °C, where $\theta = 90°$ and D_A was obtained from the initial slope of $g^{(2)}(t,q)$. The inset shows a plot on the basis of Equation 1.14, in which the intercept and the slope are D and $\langle I_d \rangle_T$, respectively. Reprinted with permission from [122], Zhao, Y., Zhang, G.Z., and Wu, C. *Macromolecules* 34, 7804, 2001. © 2001 American Chemical Society.

the sol state) due to the shrinking of individual microgels. It is worth noting that in the temperature range 15–33 °C the microgels in a dilute dispersion can reversibly swell and shrink with a size change between ~45 nm and ~106 nm, corresponding to a 13-times variation in volume. This is why the swelling could induce the sol–gel transition. Note that $\langle I \rangle_E$ increases with temperature, which is very different from previous observations in which $\langle I \rangle_E$ decreased when a physical gel melted into individual, less scattered polymer chains [123], but similar to a concentration-induced sol–gel transition. This difference can be attributed to the fact that individual collapsed microgels are stronger scattering objects than the swollen gel network in this study, especially when the temperature approaches its LCST.

For each chosen sample position at a given q, we can measure $\langle I \rangle_T$ from static LLS and calculate one D_A from $g^{(2)}(t,q)$ measured in dynamic LLS [130]. Figure 1.18 shows that D_A decreases as $\langle I \rangle_T$ increases and approaches a constant when $\langle I \rangle_T$ is sufficiently high. The inset is a corresponding plot on the basis of Equation 1.14. A least-square fitting of the data leads to D and $\langle I_d \rangle_T$, respectively, from its slope and intercept.

In the present case, individual microgels shrink so that non-jammed microgels diffuse quickly with temperature. Above the melting temperature, the gel network breaks into slowly diffused large clusters so that D decreases. Note that the value of D is close to that of individual microgels in a dilute dispersion. Since individual swollen microgels are transparent to the light used, the inhomogeneities observed in Figure 1.17 must come from an imperfect packing of the microgels when they are suddenly jammed together. Therefore, if we slow down the cooling process, the swollen microgels would have time to arrange themselves into a more uniform structure. Ideally, if individual collapsed microgels could be closely stacked together at a high temperature before cooling them down, we might be able to

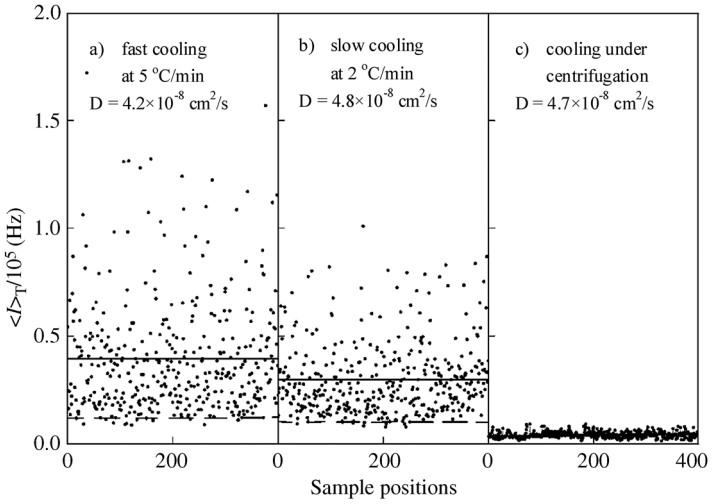

Figure 1.19 Sample position dependence of time-averaged scattered light intensity $\langle I \rangle_T$ of hybrid PNIPAM gel after the microgel dispersion was cooled down from 40 to 15 °C under different conditions, where the solid and dashed lines represent $\langle I \rangle_E$ and $\langle I_d \rangle_T$, respectively. Reprinted with permission from [122], Zhao, Y., Zhang, G.Z., and Wu, C. *Macromolecules* 34, 7804, 2001. © 2001 American Chemical Society.

obtain a uniform hybrid gel [124]. It should be stated that the hybrid gel prepared under centrifugation showed a color if a white light was shone on it even if it could not completely disperse the white light as a prism or a crystal. This imperfect dispersion might be attributed to the polydispersity in the microgel size and a low refractive index contrast between water and swollen microgel networks, but it clearly indicates a certain degree of ordering of the microgels inside the hybrid bulk gel.

Figure 1.19 shows that different cooling processes lead to different extents of inhomogeneity, reflected in the difference between $\langle I \rangle_E$ and $\langle I_d \rangle_T$. Note that Figures 1.17c and 1.19c are similar. Both display an ergodic behavior, that is, $\langle I \rangle_E = \langle I_d \rangle_T$. However, it is worth noting that they were obtained from two completely different states; namely, Figure 1.17c shows a measurement of a uniform and ergodic microgel dispersion in which individual collapsed microgels are under random Brownian motion in water, while Figure 1.19c is from a uniform hybrid gel.

Figure 1.19 clearly demonstrates that the static inhomogeneity of thermally reversible physical gels is not intrinsic but strongly dependent of the gelation process. It is also interesting to note that D is nearly a constant, indicating that the voids inside the gel network are much larger than the microgels and the gel network does not affect the relaxation of individual non-jammed microgels. As expected, for a given temperature, individual non-jammed microgels with the same size relax at the same rate. How the gel network is formed can only affect the static part, that is, $\langle I_d \rangle_T$ but not D. This point has been overlooked in the past.

1.4 Applications

Despite having a variety of interesting physical and chemical properties, synthetic gels currently find application in only a few areas, such as foods, water adsorbents, and soft contact lenses. Two main obstacles, namely, the gel shrinking/swelling speed and mechanical strength, limit their application. Much effort has been paid in the last two decades to overcome these obstacles. It is reported that the slow shrinking rate can be attributed to the formation of a hard skin layer at the very initial stage of gel shrinking, which prevents further diffusion and outflow of solvent molecules such as water molecules from inside the gel [125–127]. Using another hydrophobic polymer to modify thermally sensitive polymer gels via an interpenetrating polymer network (IPN) structure has also been reported [128, 129]. Such a gel is mainly used in drug delivery. Yoshida *et al.* [129] reported that a hydrogel modified by grafting also shows an increased shrinking rate. However, preparation of such a comb-type grafted hydrogel is not a simple task. Simple approaches are desirable to prepare polymer gel/microgel composition, which has improved shrinking rate and strength characteristics [130–133].

Spherical PNIPAM microgels with a diameter of 0.3–1.0 μm in the swollen state are embedded into a gelatin network. The shrinking of the microgels can lead the gelatin gel to shrink quickly. The embedded microgels were attached to the gelatin gel network by physical adhesion and not by chemical bonding. Therefore, it is expected that the shrunken microgels could slowly detach themselves from the gelatin gel network and be absorbed by normal tissue mechanisms, because the shrunken microgels have a diameter of only 0.1–0.3 μm. The product used here is a polymer in the form of a soft gel as shown in Figure 1.20.

The *in vivo* biological responses to the polymer gel had to be tested carefully before it could be accepted as a surgical implant. Different tissues that were likely to be put in contact with the implant when used surgically were chosen. Different tissues might have different responses to the polymer, and how the polymer would degrade with time also needed to be clarified. The tissues included subcutaneous tissues, nerve, artery, tendon, and muscle. The animals used included adult male Wistar rats and guinea pigs. Short-term and medium-term observations were made and the implant sites were inspected after periods of 3, 10, 20, and 90 days.

Polymer gel–gelatin sheet was used to wrap the cut ends of the sciatic nerve of the rat, so as to form a bridging tube. The rats were euthanized after 3, 10, 20, and 90 days to retrieve the repaired nerve for gross and histological study, as shown in Figure 1.21.

The femoral artery of the rat was used for the study of arterial repair. After cutting through, the arterial ends were prevented from separating by putting two 10 "0" stitches to sling the edges together while leaving a gap of about 1 mm open. Then the approximated site was wrapped around with a thin sheet of thermally sensitive polymer gel. The rats were euthanized on days 3, 10, 20, and 90 for the inspection and retrieval of the bridged artery (Figure 1.22).

The gel material is nontoxic. Both rats and guinea pigs survived well after the gel implantations. When the implantation sites were inspected, there was neither gross

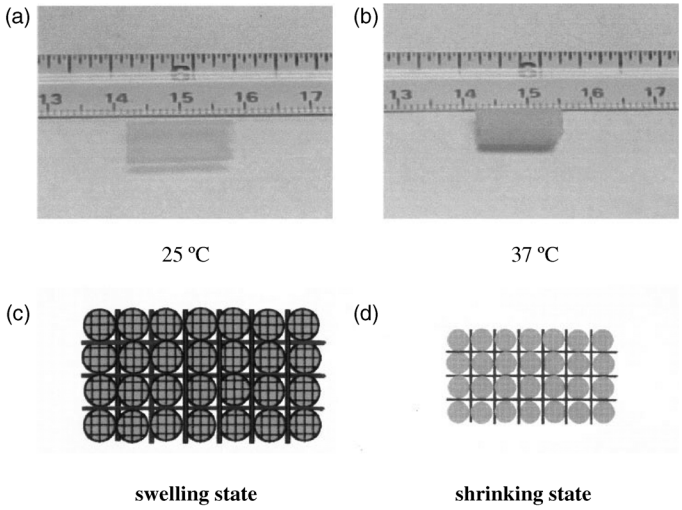

Figure 1.20 (a) Thermally sensitive polymer at 25 °C. (b) Same polymer at 37 °C. (c) Polymer at 25 °C. (d) Same polymer at 37 °C. Reprinted with permission from [134] Leung, P.C., Yew, D., Wu, C., and Peng, S.F. *Microsurgery* 23, 123, 2003. © 2003 Wiley-Liss, Inc.

nor histological suggestion of toxicity. The tissues around the implanted polymer gel were inspected for inflammatory changes and at the same time the degradation of the gel material was recorded.

The thermally sensitive polymer microgel sheet used was the product of multiple early tests, using polymers of different protein concentrations and different

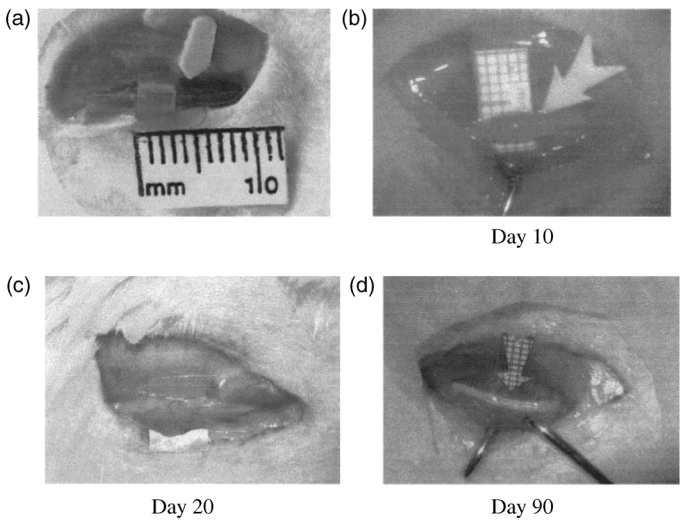

Figure 1.21 (a) Sciatic nerve of rat, bisected across, and cut ends wrapped with thermally sensitive gel. (b) Day 10. (c) Day 20. (d) Day 90. Reprinted with permission from [134], Leung, P.C., Yew, D., Wu, C., and Peng, S.F. *Microsurgery* 23, 123, 2003. © 2003 Wiley-Liss, Inc.

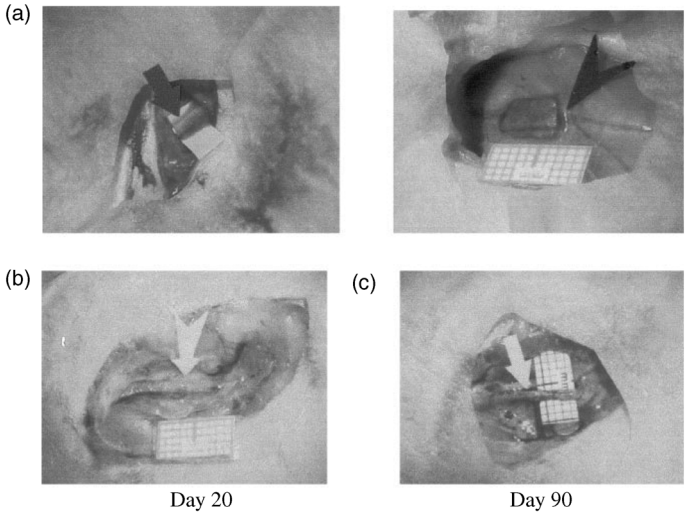

Figure 1.22 (a) Femoral artery of rat, bisected across, cut ends wrapped with thermosensitive gel. (b) Day 20. (c) Day 90. Reprinted with permission from [134], Leung, P.C., Yew, D., Wu, C., and Peng, S.F. *Microsurgery* 23, 123, 2003. © 2003 Wiley-Liss, Inc.

morphological forms, which included preformed tubes and fluid forms. The unique property of the polymer microgel is that it gives extra binding power when it is wrapped around cylindrical biological structures. The experiments on arteries and peripheral nerves showed that wrapping facilitated the maintenance of arterial patency and allowed natural nerve regeneration, while the foreign body reaction to the implanted polymer was mild.

Two more potential uses of this polymer could be considered for muscle and tendon repair. When muscle tissues are disrupted, repair by ordinary suturing gives very poor results because of extensive fibrosis around the repaired site and replacement of the damaged muscle with fibrous tissues, which leads to a gross loss of muscle function. If a tissue wrap could be applied to the damaged site to bring about approximation while minimizing fibrosis, the functional results might be better.

1.5 Conclusions

Microgels exhibit unique physical properties between those of a polymer coil and a macroscopic gel. By using a microgel as a model system, we have studied volume phase transition, internal motion, aggregation, and non-ergodic phenomena. The reason for the volume phase transition of a polymer gel is that the subchains normally have a broad chain length distribution. However, a higher homogeneity gels with a lower crosslinking density display a discontinuous volume phase transition because of the subchain inhomogeneity. The internal motion of a linear polymer chain or

microgel can be observed in good and Θ solvents at a certain observation lengths. Its nature still remains elusive but it is associated with the thermal motion of subchains.

Cations can induce the aggregation of microgels because of the interaction between the cations and anionic groups (e.g., carboxylic groups). Such a cation–polyanion complex leads to the sorting of oppositely charged microgels in a mixture; they form core–shell structures with one microgel as the core and the oppositely charged one as the shell. These cation–polyanion complexes can also induce fractal aggregates of microgels following a diffusion-limited cluster–cluster aggregation (DLCA) process. Charged microgels can form complexes with proteins, and the properties of the complexes depend on the molar ratio of protein to microgels. Thus, thermally sensitive microgels can be used in protein adsorption and separation.

The studies on the non-ergodic and ergodic phenomena of gel formed by close-packed microgels via physical interaction reveal that the observed static non-ergodicity is not intrinsic but strongly depends on how the microgels (clusters) are packed, and the dynamic fluctuation is slightly influenced by the static non-ergodicity.

The studies also show that thermally sensitive microgels have potential uses for muscle and tendon repair.

Abbreviations

Φ: Flory constant
Γ: Half-width at half-height
θ: Scattering angle
χ_T: Flory–Huggins polymer–solvent interaction parameter
$[\eta]$: Intrinsic viscosity
$<\alpha^2>_0$: Isotropic deformation factor of the gel network
D: Translational diffusion coefficient
DLCA: Diffusion-limited cluster–cluster aggregation
$g^{(2)}(t,q)$: Intensity–intensity time correlation function
IPN: Interpenetrating polymer network
LCST: Lower critical solution temperature
M_c: Average molar mass of subchain between two neighbor crosslinking points
q: Scattering vector
R_g: Radius of gyration
R_h: Hydrodynamic radius
RLCA: Reaction-limited cluster–cluster aggregation

Acknowledgments

The financial support of the National Distinguished Young Investigator Fund (20725414), National Basic Research Program of China (973 Program, 2012CB821500), and Ministry of Science and Technology of China (2012CB933800) is gratefully acknowledged. We are also indebted to Professor Chi Wu of the Chinese

University of Hong Kong, Professor Shuiqin Zhou of the City University of New York, and to Drs. Peng SF, Zhao Y, Jiang SH, Dai ZJ, and Hou Y.

References

1 Pelton, R.H. and Chibante, P. (1986) *Colloids Surf.*, **20**, 247.
2 Crespy, D. and Rossi, R.M. (2007) *Polym. Int.*, **56**, 1461.
3 Nayak, S. and Lyon, L.A. (2005) *Angew. Chem. Int. Ed.*, **44**, 7686.
4 Prokop, A., Kozlov, E., Carlesso, G., and Davidson, J.M. (2002) *Adv. Polym. Sci.*, **160**, 119.
5 Baker, W.O. (1949) *Ind. Eng. Chem.*, **41**, 511.
6 Flory, P.J. (1953) *Principles of Polymer Chemistry*, Cornell University Press, Ithaca, NY.
7 Williams, C., Brochard, F., and Frisch, H.L. (1981) *Annu. Rev. Phys. Chem.*, **32**, 433.
8 Stockmayer, W.H. (1960) *Makromol. Chem.*, **35**, 54.
9 Ptitsyn, O.B., Kron, A.K., and Eizner, Y.Y. (1993) *J. Polym. Sci. Part C*, **16**, 3509.
10 Yamakawa, H. (1971) *Modern Theory of Polymer Solutions*, Harper & Row, New York.
11 Post, C.B. and Zimm, B.H. (1979) *Biopolymers*, **18**, 1487. 21, 2123, 1982.
12 Tanaka, F. (1985) *J. Chem. Phys.*, **85**, 4707.
13 Park, I.H., Wang, Q.W., and Chu, B. (1987) *Macromolecules*, **20**, 1965.
14 Chu, B., Park, I.H., Wang, Q.W., and Wu, C. (1987) *Macromolecules*, **20**, 2883.
15 Tanaka, F. and Ushiki, H. (1988) *Macromolecules*, **21**, 1041.
16 Grosberg, A.Y. and Kuznetsov, D.V. (1992) *Macromolecules*, **25**, 1996.
17 Chu, B., Yu, J., and Wang, Z.L. (1993) *Prog. Colloid Polym. Sci.*, **91**, 142.
18 Yamakawa, H. (1993) *Macromolecules*, **26**, 5061.
19 Grosberg, A.Y. and Kuznetsov, D.V. (1993) *Macromolecules*, **26**, 4249.
20 Yu, J., Wang, Z.L., and Chu, B. (1992) *Macromolecules*, **25**, 1618.
21 Chu, B., Ying, Q.C., and Grosberg, A.Y. (1995) *Macromolecules*, **28**, 180.
22 Wu, C. and Zhou, S.Q. (1995) *Macromolecules*, **28**, 5388.
23 Wu, C. and Zhou, S.Q. (1996) *Phys. Rev. Lett.*, **77**, 3053.
24 Dusek, K. and Patterson, D. (1968) *J. Polym. Sci. Polym. Phys. Ed.*, **6**, 1209.
25 Dusek, K. and Prins, W. (1969) *Adv. Polym. Sci.*, **6**, 1.
26 Flory, P.J. (1956) *J. Am. Chem. Soc.*, **78**, 191.
27 Hermans, J.J. (1956) *J. Polym. Sci.*, **59**, 191.
28 James, H.M. and Guth, E. (1953) *J. Chem. Phys.*, **21**, 1048.
29 Tanaka, T., Sato, E., Hirokawa, Y., Hirotsu, S., and Peetermans, J. (1985) *Phys. Rev. Lett.*, **55**, 2455.
30 Hirotsu, S. (1987) *J. Phys. Soc. Jpn*, **56**, 233.
31 Hirose, Y., Hirokawa, Y., and Tanaka, T. (1987) *Macromolecules*, **20**, 1342.
32 Marchetti, M., Prager, S., and Cussler, E.L. (1990) *Macromolecules*, **23**, 3445.
33 Inomata, H., Goto, S., and Saito, S. (1990) *Macromolecules*, **23**, 4888.
34 Kokufuta, E., Zhang, Y., and Tanaka, T. (1993) *Macromolecules*, **26**, 1053.
35 Li, Y. and Tanaka, T. (1989) *J. Chem. Phys.*, **90**, 5161.
36 Shibayama, M., Morimoto, M., and Nomura, S. (1994) *Macromolecules*, **27**, 5060.
37 Park, T.G. and Hoffman, A.S. (1994) *J. Appl. Polym. Sci.*, **52**, 85.
38 Yu, H. and Grainger, D.W. (1994) *Macromolecules*, **27**, 4554.
39 Pecora, R. (1965) *J. Chem. Phys.*, **43**, 1762.
40 Perico, A., Piaggio, P., and Cuniberti, C. (1975) *J. Chem. Phys.*, **62**, 2690.
41 Perico, A., Piaggio, P., and Cuniberti, C. (1975) *J. Chem. Phys.*, **62**, 4911.
42 Sorlie, S.S. and Pecora, R. (1988) *Macromolecules*, **21**, 1437.

43 Zimm, B.H. (1956) *J. Chem. Phys.*, **24**, 269.

44 Zimm, B.H. and Roe, G.M. (1956) *J. Chem. Phys.*, **24**, 279.

45 Wang, J., Wang, Z.L., Peiffer, D.G., Shuely, W.J., and Chu, B. (1991) *Macromolecules*, **24**, 790.

46 Wu, C. and Xia, K. (1994) *Q. Rev. Sci. Instrum.*, **65**, 587.

47 Wu, C. and Zhou, S.Q. (1996) *J. Polym. Sci. Polym. Phys.*, **34**, 1597.

48 Adam, M., Delsanti, M., Munch, J.P., and Durand, D. (1988) *Phys. Rev. Lett.*, **61**, 706.

49 Martin, J.E. and Wilcoxon, J. (1988) *Phys. Rev. Lett.*, **61**, 373.

50 Shibayama, M. (1998) *Macromol. Chem. Phys.*, **199**, 1.

51 Shibayama, M. and Norisuye, T. (2002) *Bull. Chem. Soc. Jpn.*, **75**, 641.

52 Ngai, T., Wu, C., and Chen, Y. (2004) *Macromolecules*, **37**, 987.

53 Pusey, P.N. and van Megen, W. (1989) *Physica A*, **157**, 705.

54 Joosten, J.G.H., Mccarthy, J.L., and Pusey, P.N. (1991) *Macromolecules*, **24**, 6690.

55 Tanaka, T., Hocker, L.O., and Benedek, G.B. (1973) *J. Chem. Phys.*, **59**, 5151.

56 Horkay, F., Burchard, W., Hecht, A.M., and Geissler, E. (1993) *Macromolecules*, **26**, 3375.

57 Asnaghi, D., Carpineti, M., Giglio, M., and Sozzi, M. (1992) *Phys. Rev. A*, **45**, 1018.

58 Fernandez-Barbero, A., and Vincent, B. (2000) *Phys. Rev. E*, **63**, 011509.

59 Robinson, D.J. and Earnshaw, J.C. (1992) *Phys. Rev. A*, **46**, 2045.

60 Cheng, H., Wu, C., and Winnik, M.A. (2004) *Macromolecules*, **37**, 5127.

61 Wu, C., Zhou, S.Q., Au-yeung, S.C.F., and Jiang, S.H. (1996) *Die Angew. Makromol. Chem.*, **240**, 123.

62 Wu, C. and Zhou, S.Q. (1997) *J. Macromol. Sci. Phys. B*, **36**, 345.

63 Gao, J. and Wu, C. (1997) *Acta Polym. Sin.*, **3**, 324.

64 Wu, C. (1998) *Polymer*, **39**, 4609.

65 Wu, C. and Zhou, S.Q. (1997) *Macromolecules*, **30**, 574.

66 Wu, C. and Yan, C.Y. (1994) *Macromolecules*, **27**, 4516.

67 Dai, Z.J., Ngai, T., and Wu, C. (2011) *Soft Matter*, **7**, 4111.

68 Wu, C. and Zhou, S.Q. (1996) *Macromolecules*, **29**, 1574.

69 Wu, C., Chan, K.K., and Xia, K. (1995) *Macromolecules*, **28**, 1032.

70 Dai, Z.J. and Wu, C. (2010) *Macromolecules*, **43**, 10064.

71 Peng, S.F. and Wu, C. (2012) In *Handbook of Polyelectrolytes and Their Applications*, Vol. 2: *Polyelectrolytes: their Characterization and Polyelectrolyte Solutions* (eds S.K. Tripathy, J. Kumar, and H.S. Nalwa), American Scientific Publishers, CA, chapter 7, pp. 189–225.

72 Peng, S.F. and Wu, C. (2001) *J. Phys. Chem. B*, **105**, 2331.

73 Stockmayer, W.H., and Schmidt, M. (1982) *Pure Appl. Chem.*, **54**, 407.

74 Hirokawa, Y. and Tanaka, T. (1984) *J. Chem. Phys.*, **81**, 6379.

75 Ershov, B.G. and Henglein, A. (1998) *J. Phys. Chem. B*, **102**, 10663.

76 Ikeda, Y., Beer, M., Schmidt, M., and Huber, K. (1998) *Macromolecules*, **31**, 728.

77 Heitz, C. and Francois, J. (1999) *Polymer*, **40**, 3331.

78 Frank, H.S. and Wen, W.Y. (1978) *Discuss. Faraday Trans.*, **74**, 583.

79 James, D.W. and Frost, R.L. (1978) *J. Chem. Soc., Faraday Trans.*, **74**, 583.

80 Hindman, J.C. (1962) *J. Chem. Phys.*, **36**, 1000.

81 Peng, S.F. and Wu, C. (2001) *Macromolecules*, **34**, 6795.

82 Peng, S.F. and Wu, C. (2001) *Polymer*, **42**, 6871.

83 Hou, Y., Ye, J., Wei, X.L., and Zhang, G.Z. (2009) *J. Phys. Chem. B*, **113**, 7457.

84 Kabanov, V.A. and Zezin, A.B. (1985) *Pure Appl. Chem.*, **56**, 343.

85 Thomas, J.L., Brian, P.D., and Tirrell, D.A. (1996) *Biochim. Biophys. Acta*, **1278**, 73.

86 Bondeson, J. and Sundler, R. (1990) *Biochim. Biophys. Acta*, **1026**, 186.

87 Kuber, K. (1993) *J. Phys. Chem.*, **97**, 9825.

88 Peng, S.F. and Wu, C. (2001) *Polymer*, **42**, 7343.

89 Meakin, P. (1983) *Phys. Rev. Lett.*, **51**, 1119.

90 Martin, J.E. and Ackerson, B. (1985) *J. Phys. Rev. A*, **31**, 1180.

91 Jullien, R., Botet, R., and Mors, P.M. (1987) *Faraday Disuss. Chem. Soc.*, **83**, 125.

92 Reinecke, H., Fazel, N., Dosiere, M., and Guenet, J.M. (1997) *Macromolecules*, **30**, 8360.

93 Aubert, C. and Cannell, D.S. (1986) *Phys. Rev. Lett.*, **56**, 738.

94 Lin, M.Y., Lindsay, H.M., Weitz, D.A., Ball, R.C., Klein, R., and Meakin, P. (1989) *Nature*, **40**, 4665.

95 Micali, N., Mallamace, F., Romeo, A., Purrello, R., and Scolaro, L. (2000) *J. Phys. Chem. B*, **104**, 5897.

96 Magazu, S., Maisano, G., Mallamace, F., and Micali, N. (1989) *Phys. Rev. A*, **39**, 4195.

97 Botet, R., Kolb, M., and Jullien, R. (1985) *Physics of Finely Divided Matter*, Springer-Verlag, New York.

98 Zhou, Z. and Chu, B. (1991) *J. Colloid Interface Sci.*, **143**, 356.

99 Aymard, P., Nicolai, T., Durand, D., and Clark, A. (1999) *Macromolecules*, **32**, 2542.

100 Kim, A.Y. and Berg, J.C. (2000) *Langmuir*, **16**, 2101.

101 Takata, S., Norisuye, T., Tanaka, N., and Shibayama, M. (2000) *Macromolecules*, **33**, 5470.

102 Larson, R.G. (1999) *The Structure and Rheology of Complex Fluids*, Oxford University Press, New York, chapter 5, pp. 232–258.

103 Lapasin, R. and Pricl, S. (1998) In *Progress and Trends in Rheology Vol. V the Fifth European Rheology Conference* (eds Emri, I. and Cvelbar, R.), Springer, Berlin, pp. 22.

104 Winter, H.H. (2007) In *Encyclopedia of Polymer Science and Engineering*, Third Edition, John Wiley & Sons, Inc., New York, pp. 507.

105 Almdal, K., Dyre, J., Hvidt, S., and Kramer, O. (1993) *Polym. Gels Networks*, **1**, 5–17.

106 Wu, C., Zuo, J., and Chu, B. (1989) *Macromolecules*, **22**, 633.

107 Sato-Matsuo, E., Orkisz, M., Sun, S.T., Li, Y., and Tanaka, T. (1994) *Macromolecules*, **27**, 6791.

108 Wu, C., Chu, B., and Stell, G. (1989) *Makromol. Chem., Macromol. Symp.*, **45**, 75.

109 Norisuye, T., Inoue, M., Shibayama, M., Tamaki, R., and Chujo, Y. (2000) *Macromolecules*, **33**, 900.

110 Brown, W. (1993) *Dynamic Light Scattering, the Methods and Applications;*, Clarendon Press, Oxford.

111 Panyukov, S. and Rabin, Y. (1996) *Macromolecules*, **29**, 7690.

112 Panyukov, S. and Rabin, Y. (1996) *Phys. Rep.*, **269**, 1.

113 Horkay, F., Hecht, A.M., Mallam, S., Geissler, E., and Renie, A.R. (1991) *Macromolecules*, **24**, 2896.

114 Shibayama, M., Tanaka, T., and Han, C.C. (1992) *J. Chem. Phys.*, **97**, 6892.

115 Rouf, C., Bastide, J., Pujol, J.M., Schosseler, F., and Munch, J.P. (1994) *Phys. Rev. Lett.*, **73**, 830.

116 Bastide, J. and Leibler, L. (1988) *Macromolecules*, **21**, 2647.

117 Hecht, A.M., Duplessix, R., and Geissler, E. (1985) *Macromolecules*, **18**, 2167.

118 Mallam, S., Horkay, F., Hecht, A.M., and Geissler, E. (1989) *Macromolecules*, **22**, 3356.

119 Cohen, Y., Ramon, O., Kopelman, I.J., and Mizrahi, S.J. (1992) *Polym. Sci., Polym. Phys. Ed.*, **30**, 1055.

120 Joosten, J.G.H., Gelade, E., and Pusey, P.N. (1990) *Phys. Rev. A*, **42**, 2161.

121 Fang, L. and Brown, W. (1992) *Macromolecules*, **25**, 6897.

122 Zhao, Y., Zhang, G.Z., and Wu, C. (2001) *Macromolecules*, **34**, 7804.

123 Ikkai, F. and Shibayama, M. (1999) *Phys. Rev. Lett.*, **82**, 4946.

124 Zhao, Y. and Wu, C. (2002) *Chinese J. Polym. Sci.*, **20**, 269.

125 Gutowska, A., Bae, Y.H., Feijen, J., and Kim, S.W. (1992) *J. Controlled Release*, **22**, 95.

126 Yoshida, R., Sakai, K., Okano, T., and Sakurai, Y. (1994) *J. Biomater. Sci. Polymer Ed.*, **6**, 585.

127 Kim, Y.H., Bae, Y.H., and Kim, S.W. (1994) *J. Controlled Release*, **28**, 143.

128 Gutowska, A., Bae, Y.H., Jacobs, H., Feijen, J., and Kim, S.W. (1994) *Macromolecules*, **27**, 4167.

129 Yoshida, R., Uchida, K., Kaneko, Y., Sakai, K., Kikuchi, A., Sakurai, Y., and Okano, T. (1995.) *Nature*, **374**, 240.
130 Wu, C. and Jiang, S.H. (2000) U.S. Patent No. 6,030,634. Approved on February 29.
131 Wu, C. and Jiang, S.H. (2001) U.S. Patent No. 6,238,688. Approved on May 29.
132 Wu, C. and Jiang, S.H. (2003) Chinese Patent No. 97 1 80823.6. Approved on March 5.
133 Wu, C. and Jiang, S.H. (2003) HK Standard Patent No. 1025585. Approved on September 19.
134 Leung, P.C., Yew, D., Wu, C., and Peng, S.F. (2003) *Microsurgery*, **23**, 123.